

PAPER

## Laser pyrolysis for controlled morphing and chemical modification on 3D microlattices

To cite this article: Zacharias Vangelatos *et al* 2020 *J. Micromech. Microeng.* **30** 055008

View the [article online](#) for updates and enhancements.



**IOP | ebooks™**

Bringing together innovative digital publishing with leading authors from the global scientific community.

Start exploring the collection—download the first chapter of every title for free.

# Laser pyrolysis for controlled morphing and chemical modification on 3D microlattices

Zacharias Vangelatos<sup>1,2,3</sup> , Letian Wang<sup>1,2,3</sup> and Costas P Grigoropoulos<sup>1,2</sup> 

<sup>1</sup> Department of Mechanical Engineering, University of California, Berkeley, California 94720, United States of America

<sup>2</sup> Laser Thermal Laboratory, University of California, Berkeley, California 94720, United States of America

E-mail: [cgrigoro@berkeley.edu](mailto:cgrigoro@berkeley.edu)

Received 27 December 2019, revised 10 February 2020

Accepted for publication 4 March 2020

Published 16 April 2020



## Abstract

3D microlattices fabricated through multi-photon lithography have been widely utilized for photonics, bio-scaffolds and architected metamaterials. Post-processing techniques have accentuated the reduction of the overall size to the nanoscale and the modification of the material properties of these structures. However, there are no processing techniques that can locally modify the morphology and the properties of microscale polymeric structures. In this study, our objective is to demonstrate localized nanoscale morphing and material modification of polymer 3D lattice structures through continuous wave laser induced selective pyrolysis, leading to local carbonization. Our approach of focused laser heating on single beam members precipitates thickness reduction from 500 nm to 250 nm. Local size reduction can further embrace collective mechanical deformation and form new complex geometries. Through spatially-variant laser heating on the periodic structures, curved and gradient three-dimensional shapes can be fabricated. Finite element analysis explained the resulted changes and predicted the enhanced mechanical performance. Ultimately, *in situ* scanning electron microscopy of the microindentation process proves that the modified structure demonstrates a substantially improved mechanical performance through the combination of high strength and ductility of the ceramic and polymer counterparts. Our findings and main results demonstrate the significance of the laser as a vital tool to ameliorate the geometrical complexity and material heterogeneity for enhanced mechanical performance.

Supplementary material for this article is available [online](#)

Keywords: 3D microlattices, laser extreme pyrolysis, hybrid material, mechanical metamaterial, multi-photon lithography, post-processing, Helium Ion Microscopy

(Some figures may appear in colour only in the online journal)

## 1. Introduction

Micro/nanolattice structures possess enhanced properties bestowed by their tailored structure. Their utility can be employed for various different applications, including ultra-light, ultra-stiff structures for structural materials [1, 2],

controlled wave propagation [3], lithium-ion batteries [4] and even 3D piezoelectric microstructures [5, 6]. In addition, these architected designs can also be employed for bio-tissue engineering as meta-implants [7] or cardiac tissue that can be engineered to study cardiac diseases [8]. Novel designs can also be utilized for bone tissue engineering to investigate how nano and micro structural features provide high strength and energy dissipation [9]. Characteristic instantiations of this

<sup>3</sup> The authors contributed equally to this work.

principle are observed in the bone microstructure [10–12], armor protection [13] of living organisms and even marine diatoms [14]. This principle is also observed in the crystal structure, through the gradient microstructure of metals, rendering them damage tolerant [15]. Therefore, nature is a celebrated paradigm that has proven the necessity of ‘smaller but stronger’ features in a functional structure. All of these advances have been accomplished by the inexorable progress in high-resolution additive manufacturing techniques, such as Multi-Photon Lithography (MPL) [16, 17]. MPL is considered the paragon of high-resolution fabrication of complex geometries, reaching feature sizes up to the nm regime [18]. The late progress in mesoscale printing provides the potential utility of MPL for large scale engineering applications, encompassing nanometer structural features [19].

Further reduction of the fabrication resolution has been accomplished by two direct fabrication techniques. One method is the Diffusion-Assisted High-Resolution Direct Femtosecond Laser Writing [15], accomplishing 60 nm structural features in woodpile structures. The second one is the Stimulated Emission Depletion (STED), combined with Direct Laser Writing (DLW). This technique has provided simple 3D cubic structures with lattice members consisting of 55 nm thickness [20]. Nevertheless, both of these techniques have not been successfully employed for the fabrication of complex metamaterial structures, such as the octet truss (OT) or the cuboctahedron (CB) [21], with such miniscule lattice thickness.

Post processing methods introduce both size reduction and chemical modification, with most notable examples being plasma etching [22] and pyrolysis [18]. Before utilizing oxygen plasma etching, a metal must be initially deposited on the fabricated structures. Afterwards, etching of the internal polymer core also oxidizes the metal and hollow ceramic nanolattices with thickness from 5 to 60 nm can be fabricated [23]. These nanostructures have unprecedented resilience and recoverability to large deformations, even though they are ceramic.

Moreover, pyrolysis can provide remarkable uniform shrinkage of the photopolymerized structure, reaching strut thickness up to 200 nm and isotropic shrinking up to 80%. Besides the size reduction, the photosensitive polymeric material is also thermally decomposed, forming a glassy carbon structure [24]. These glassy nanolattices can reach the theoretical limit of the strength of bulk glassy carbon [25]. Raman characterization of this process reveals that the molecular vibrations which can be associated with the carbon–carbon, carbon–oxygen, and carbon–hydrogen bonds significantly differ between pyrolyzed and untreated structures. High temperature annealing leads to the creation of cristobalite and tetragonal zirconia (t-ZrO<sub>2</sub>), which are components typical for silica glass. The formation of polycrystalline silica and zirconia, in conjunction with the substantial decrease in the diameter of the lattice members insinuates that the polymer part of the photoresist is removed, while the ceramic part remains [18]. Furthermore, mechanical testing on the post-processed nanolattices has shown that they exhibit strength-to-density ratios in the same order of magnitude as

bulk diamond [25]. For further chemical modification, processes such as electroless plating [26] or ALD coating [27] can be utilized. By creating a metallic film that covers the structural members, these structures can become conductive [4] or have significant changes in their mechanical response [26]. In addition, electrochemical modification of metamaterial structures has been realized, demonstrating chemomechanically reconfigurable structures [28]. More specifically, through lithiation of the fabricated cubic lattices, buckling commences due to chemomechanical effects, creating complex reconfigurable features.

Localized structural alteration and chemical composition modification is indispensable for the design and analysis of enhanced mechanical metamaterials. Localized shape modification could potentially enhance the complexity of the fabricated structures and provide geometries that could not be fabricated efficiently with the MPL due to their proximity. The reason is that the voxels created by the laser beam intersect with each other, rendering parts of the structure indiscernible. Moreover, localized chemical composition modification can introduce local defects, which are proved to improve the mechanical performance [29]. More specifically, architected defects can be utilized for controllable deformation in lattice materials and artificial macroscopic grains for localized plasticity [30]. These defects tend to even create band gaps in the material [31] hindering the wave propagation at specific wavenumbers. However, despite their significance, all of the aforementioned methods provide uniform isotropic processing on the geometry and chemical composition. Hence, there is no reported processing method that enables the local modification on the geometry and the chemical composition of specific structural members in architected materials.

Laser extreme pyrolysis has the potential to introduce localized shaping and chemical modification through carbonization. Laser selective pyrolysis has been employed for patterning silicon carbide bulk [32], metal-organic superconducting thin films [33] or polymer thin films. Furthermore, it can effectively pattern 2D polymer structures for graphene-based applications [34, 35]. However, none of them have been utilized for shaping and modifying 3D polymer structures. The high spatial resolution and energy tunability of the laser could potentially precipitate pyrolysis on 3D polymer structures.

In this study, we demonstrate the laser localized extreme pyrolysis of polymer microlattices. First, localized modification is presented on one single beam with chemical composition mapping. Next, it is shown that localized shrinking can generate collective mechanical deformation and form new geometries on 3D unit cells such as the OT and the first stellation of rhombic dodecahedron (FS) [36]. Highly curved and twisted structures are fabricated, which are a conundrum with conventional MPL. Finally, with controlled continuous wave (CW) laser irradiation at specific positions and directions, gradient deformation can be introduced on periodic microlattices. Through heat transfer simulations, we elucidate the underlying mechanisms and provide a design approach to architect the modified structures. The mechanical performance of deformed structures is also predicted through finite element analysis (FEA). Finally, by performing in-situ scanning

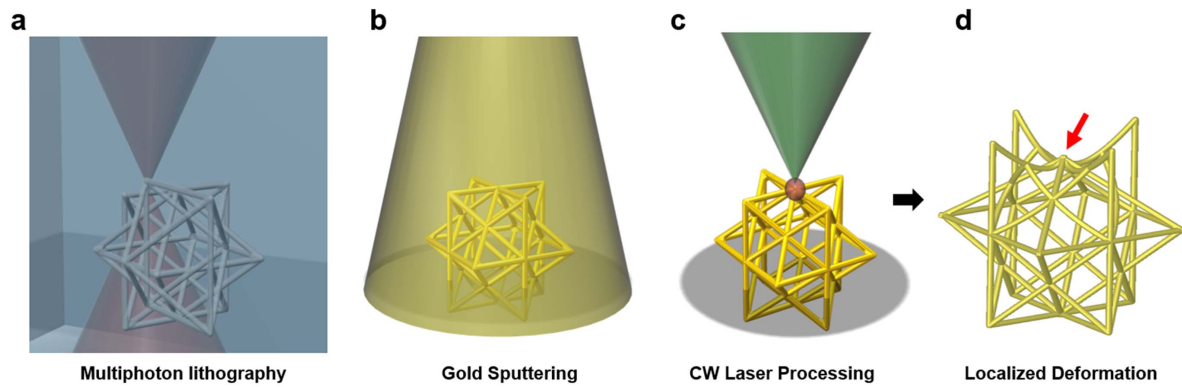


**Figure 1.** The proposed process of the laser site selective modification of MPL fabricated 3D structure. (a) Multiphoton lithography. (b) Gold sputtering to enhance absorption, a step which is optional depending on the employed laser power and pulse regimes. (c) The focused laser beam heating at the top of the 3D structure, which is labelled with a red sphere. (d) Laser heating induced gradient volume reduction and the resulted gradient structure. The upper half of the structure is shrunk and the upper beam members are curved.

electron microscopy (SEM) on microindentation testing, we delineate how a 3D hybrid, partly ceramic, partly polymeric hybrid structure [37] can have enhanced mechanical performance due to the combination of structural features and its composite nature.

## 2. Results and Discussion

The experimental procedure of the laser selective morphing of the polymer structure is depicted in figure 1. The femtosecond pulsed laser is used to induce MPL inside a photosensitive resin, whereas the photoexcited structure is developed to form a polymerized microstructure. To convey this, a simple FS structure unit cell is schematically shown as the sample. Then the polymerized structure is sputtered with gold to enhance the absorbance of the micro lattices, which is recommended for the CW laser processing. If no sputtering is applied, the shrinking requires either wavelength below 300 nm [38] or short pulses (<1 ms) and the power threshold is more narrow. Preliminary tests conducted using a nanosecond laser showed that the controllability of the shape of the structure is substantially mitigated and the power threshold is limited. Since these methods increase the complexity of the process to obtain the optimum parameters, the CW laser processing was selected. When the CW laser is focused on the prepared sample, the polymer is subject to high temperature heating and localized carbonization. The decomposition of the material and the evaporation of the gaseous phase introduces shrinkage of the structure, encompassed by deformation. When the laser heating is spatially distributed in a controlled fashion, then the tailored deformation is evinced (figure 1(d)).

Detailed geometry and chemical composition changes are characterized on simple structures (figures 2(a)–(d)) to fathom the associated mechanisms. The length of the triangular beams is 20  $\mu\text{m}$  and their thickness is approximately 500 nm. Laser irradiation on a single member of the structure leads to the local shrinking of this individual member, whose deformation can be observed from both side view and top view. EDS analysis on heated and unheated structures reveals that the laser

heating causes changes in the chemical composition of the material (figure 2(d)). We observe a significant decrease of carbon content from 41% to 23% on the heated member compared to the non-heated ones. Even though the content of all the other elements is increased in the heated area, their relative ratio remained constant. It is proposed that conventional carbonization occurs, decomposing the long polymer chains into small volatile hydrocarbon, which evaporated into the ambient air, subsequently reducing the carbon content. Excessive heating on the structures can lead to significant melting and material removal of the polymer. To forestall melting in the structures, the power of the laser beam was optimized to be 5 mW.

On microlattice unit cells, local size reduction can usher collective mechanical deformation and the formation of new geometries. Both individual OT and FS unit cells are processed and the modified unit cells are presented in figure 2(e)(i). The height of the unit cells is designed to be 10  $\mu\text{m}$  with slight deviations caused by the alignment of the MPL during the fabrication process. First, it is elucidated in figures 2(i)–(g) through both top view (i) and side view (ii) that the deformation is controllable for different laser powers. In the case of figures 2(f) and (g), the laser beam is focused on the top plane and at the center of the unit cell. Hence, a larger deformation is observed on the top plane combined with an overall contraction towards the center. This caused the shape formation of an ‘octopus jaw’ structure, which could be potentially utilized for material grasping and collection of particles on a surface [39]. As for the FS, it is observed that the location of the laser heating with respect to the geometry of the unit cell has a significant affect to the overall geometry deformation. In addition, it created a heating induced undulated morphology. All these convoluted designs with both soupçon diameter and intrinsic curvatures in close proximity are too challenging to be fabricated with conventional MPL only, such as figures 2(f)(ii) and (iv). Beams this thin in such a close proximity cannot be distinguished as separate voxels, and their fabrication cannot be successfully realized by the MPL.

Furnace pyrolysis is compared to the laser extreme pyrolysis on periodic microlattices. The fabricated FS and OT arrays are presented in figure 3(a). The FS array contains three

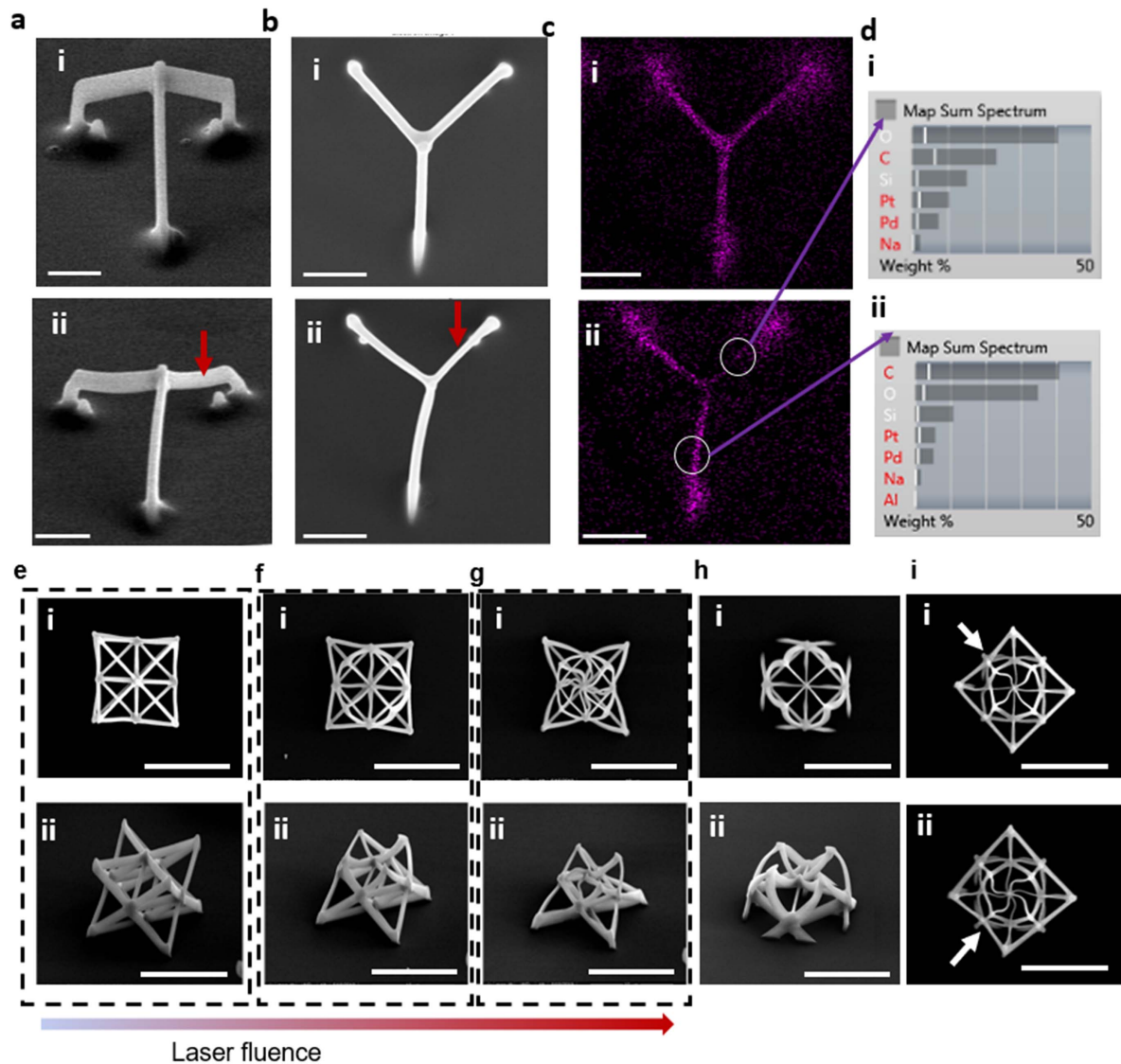


**Figure 2.** Geometry and chemical composition analysis of laser pyrolyzed simple unit cell structures. (a)–(b) tilted (a) and top view (b) of simple tetrahedral structures before (i) and after (ii) receiving selective laser heating on the arrow pointed location. (c) EDS composition mapping of the carbon concentration over the microstructure. (d) point composition analysis on structures with (i) and without (ii) laser processing. (e)–(g) top (i) and tilted view (ii) laser processed OT structure with increasing laser power from 0 mW to 5 mW and 8 mW. (h) laser heated OT with the bottom part of the structure not printed due to alignment of the height. (i) top view of the laser point heated FS structure at different locations labelled with arrows. For all of the figures the white scale bar is 10  $\mu\text{m}$ .

layers in total, with 4 ( $2 \times 2$ ) unit cells on each layer. The OT array consists of four layers, with  $4 \times 4$  unit cells on each layer. The initial diameter of the beam members is approximately 550 nm (figure S1(A) on the supplementary information (SI) (<https://stacks.iop.org/JMM/30/055008/mmedia>)). The diameter of the beam members due to laser heating drop to 250 nm (figure S1(B)), a result congruous to the reported values of the pyrolysis technique [18]. Putting these values into perspective, furnace heating causes shrinking on the same order of magnitude ( $\sim 230$  nm in diameter) (Figure S1(C)). Longer and more uniform heating introduces more volume reduction in the furnace. Tests on polymer structures under different furnace temperatures indicated that the shrinking temperature threshold is approximately 375  $^{\circ}\text{C}$ . Nevertheless, it leads to a uniform isotropic deformation in both OT and

FS. Most notably, for the OT array, except for the stepwise transition at the bottom part of the structure, the overall size reduction is uniform. Therefore, the desired localization of induced defects cannot be embraced by furnace heating.

Furthermore, we show that controlled laser carbonization can generate gradient deformation and form functional periodic microlattices. More specifically, the FS structure is converted to a ‘ziggurat’ array, whereas each layer has different height and width caused by the different degree of shrinkage in the beams. This deformation leads to a completely new design. As it will be shown later, this design embosoms significantly enhanced mechanical properties compared to the initial one. To put this result into perspective, long dwell time ascertains that gradient heating with Gaussian planar distribution is established at each vertical layer,

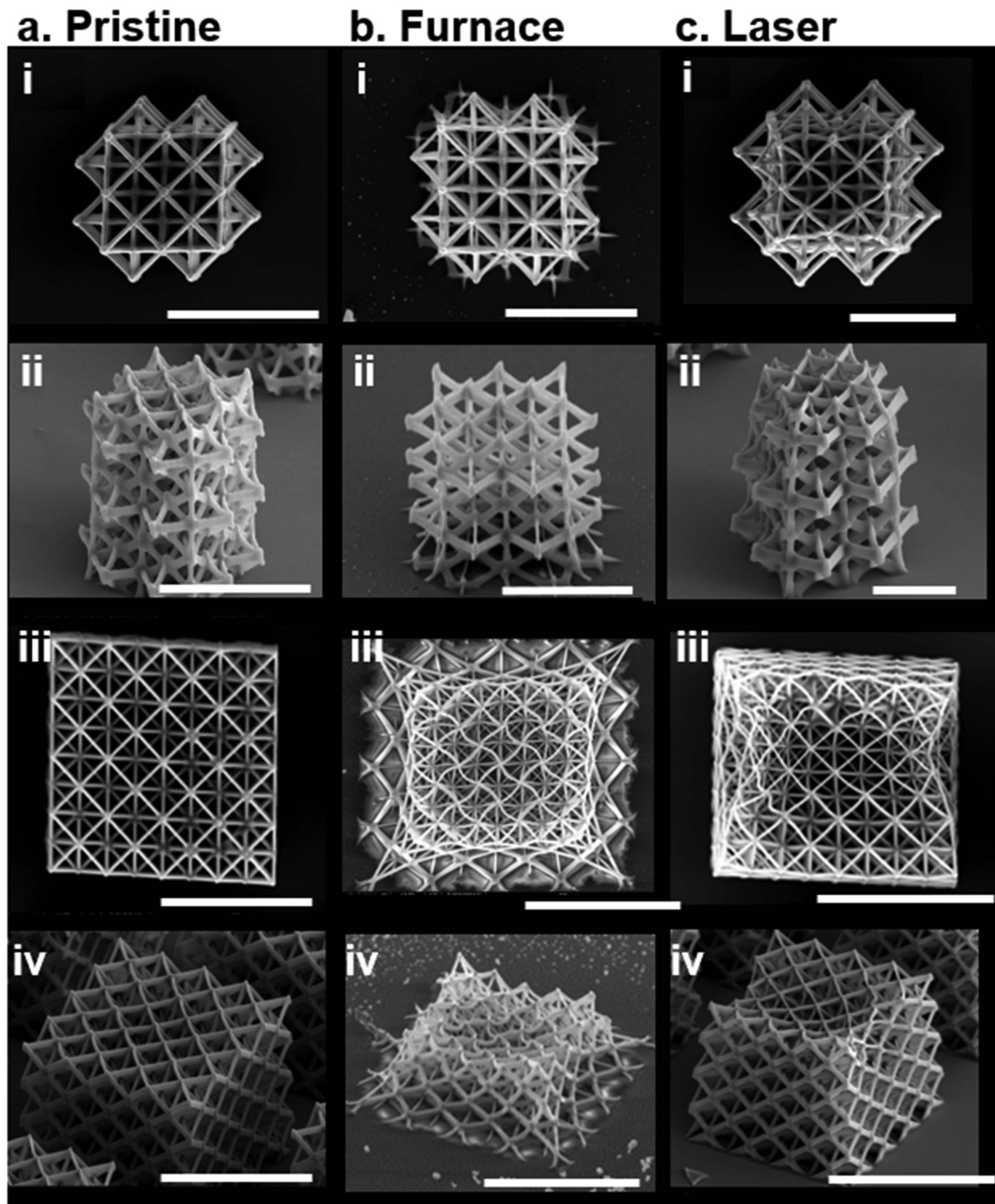


**Figure 3.** Comparison of the laser extreme pyrolyzed polymer microstructures with pristine and furnace pyrolyzed ones. (a) Pristine fabricated FS (i)–(ii) and OT (iii)–(iv) microstructure with top view and perspective isometric view. (b) Furnace processed FS and OT structure with uniform deformation. (c) Laser extreme pyrolyzed FS and OT structure. FS structure is processed by a fixed laser beam (labelled with dashed lines) heating and formed forming a zigzag structure. OT structures are heated by a scanning laser beam (in the direction of arrow) and formed a concave surface. The minimum thickness of the lattices for this case is 223 nm. The white scale bars for all of the top and side views are 10  $\mu\text{m}$ .

thus leading to the vertical gradient deformation. For the case of the OT, as the laser is scanning through the structure, a nonuniform heating and subsequent gradient deformation is formed in the same layer. As the OT is established as one of

the best ultralight-ultrathin microlattice mechanical metamaterials, this design can be employed as protection layers for micro-optical devices, where smooth alignment in an undulated profile might be design requirement [40].

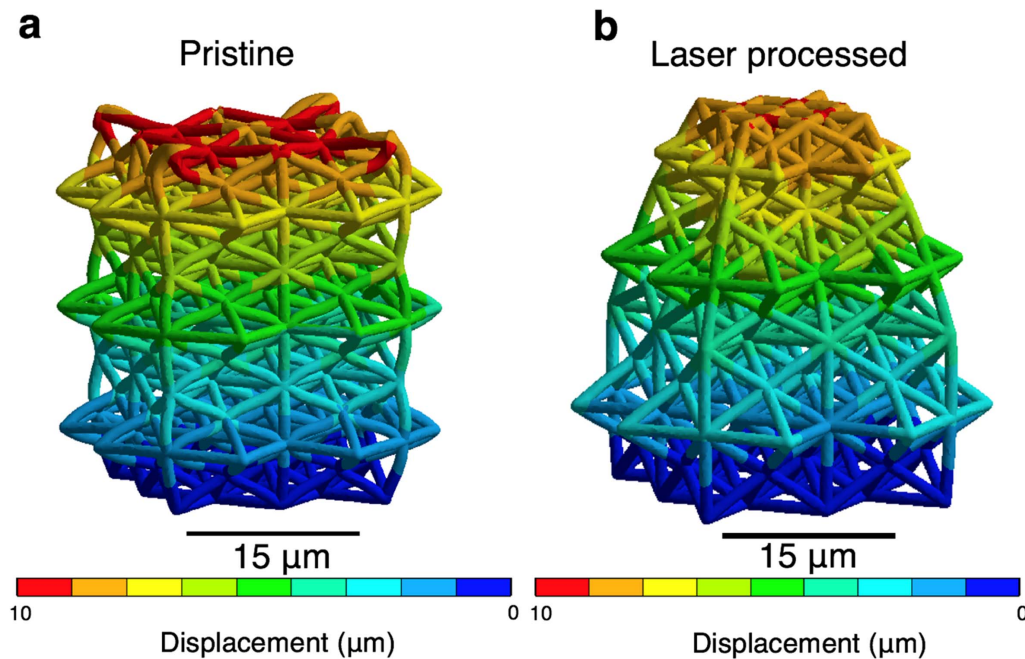


**Figure 4.** Mechanical simulations of the FS structure. The mechanical deformation profile for the pristine (a) and the laser processed (b) structures, demonstrating the resilience of the second over the first to large compression.

The correlation between the laser parameters and the deformation can be constructed and can provide the guidelines to design the desired geometries. To investigate the thermal effects, heat transfer simulations were conducted on an FS array using COMSOL. The simulated temperature distribution is presented in figure S2(i). Further details regarding the simulation parameters and results are provided in the SI. The temperature distribution appears to drop approximately linearly with the distance from the top surface as a steady distribution is established. Geometrical transitions and joints to proximal lattice members lead to a change of the temperature slope (i.e. change of the heat flux that is partially diverted to adjacent lattice members), (figures S2(ii)–(iv)). These results show that the effect of the laser is diminished through subsequent layers of lattice members in the structure, elucidating the reason for the localized deformation. The current laser input simulates the case where only initial deformation exist on the top layer of FS, where temperature is higher than 375 °C. Based on the steady state equilibrium, when the laser fluence increases, the normalized temperature distribution will still follow the simulated distribution. Therefore, when the laser fluence is increased, the deformed regions will proliferate from the top to the entire domain following the simulated temperature gradient. This phenomenon elucidates the formation of the ‘zig-zurat’ FS microlattice. Once the temperature distribution over each lattice member is attained, we can obtain the spatial distribution of the deformation, and predict the resulted geometry. Thus, a physical model connecting the laser input and the resulted geometry is constructed. It is then possible to generate optimization algorithms to do the inverse problem, i.e. calculating the required laser heating spot and power to generate the targeted geometry. It must be noted that in the above arguments, we have verified that the pyrolysis is completed on the

heated layers, in a time scale much shorter than the laser dwell time, as it is presented in the SI. For more complex deformation control, the temperature dependent shrinking speed can be investigated from refined furnace or laser heating experiments.

FEA simulations are further employed to predict the mechanical performance. To be consonant with the laser processing, the stiffness of the laser heated structure has a gradient, based on the measured mechanical properties that will be presented next. Further details are also provided in the Methods, Section 3. The force-displacement responses of the unheated and heated specimens are compared in figure 4. It is observed that the heated specimen is much more resilient to large deformations. The reason is that the maximum deformation field distribution (colored red) is substantially secluded on the top face of the heated structure. A potential reason for this phenomenon is that the top beams are closer to each other leading to a stiffer structure. This mechanism has been reported before for the case of pyrolysis [41], as the uniform shrinking reconfigures the beams to closer proximity to each other. This mechanism is manifested on the laser heated specimen as well. Nevertheless, the bottom layers are not affected, as the deformation field for both structures is the same at this location. This insinuates that the heated structure is comprised of two parts. A stiff, non-polymeric part at the top and a polymeric backbone on the bottom that can facilitate buckling and larger deformations with plasticity before fracture [26, 37]. This will be verified by both the mechanical testing that will be presented next and EDS analysis on the cross sections of heated and unheated lattices. Therefore, this process can be employed to create materials encompassing both strength and ductility. These results, synergistically coupled with the simulation of the mechanical behavior, can be employed to design the laser processing towards the desired mechanical performance.

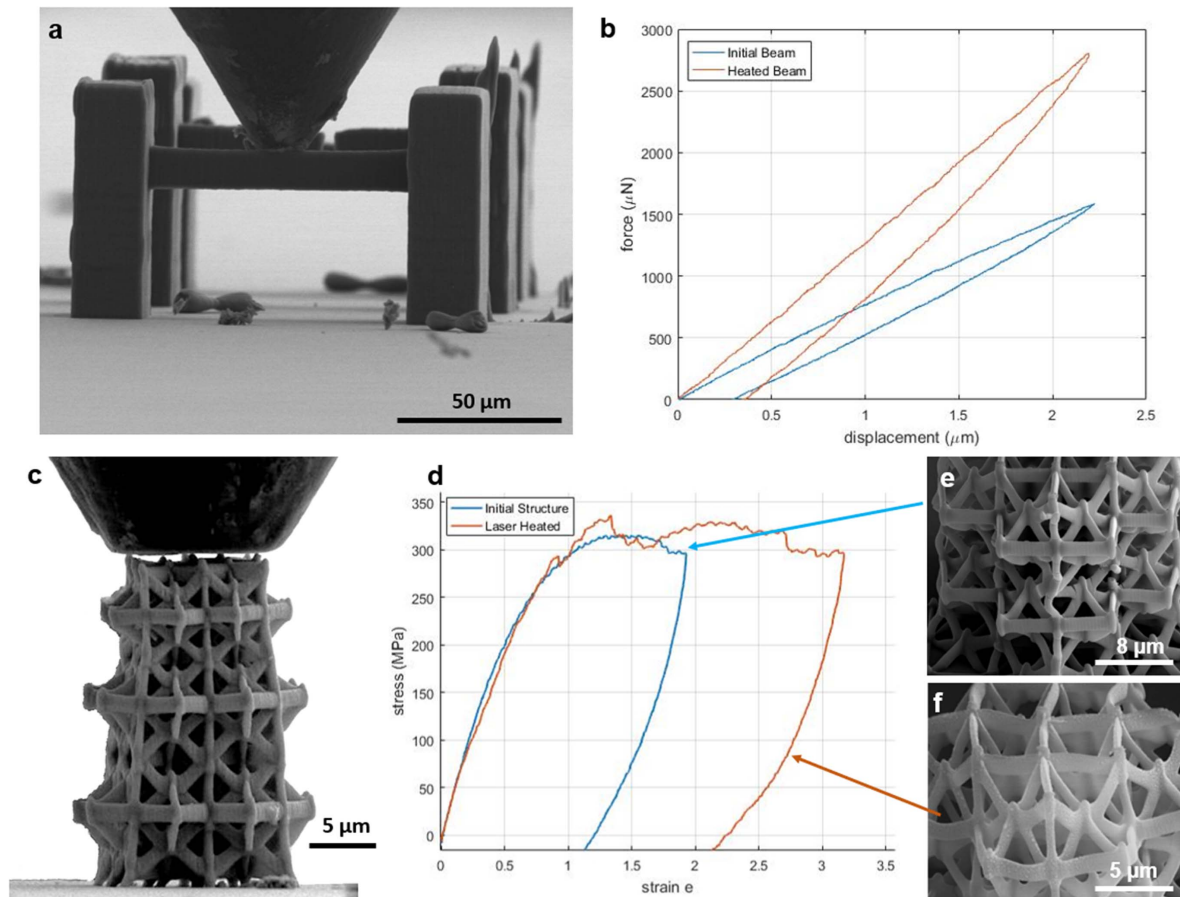


**Figure 5.** Micro-indentation testing of the initial and laser carbonized structures. (a) Front view of characteristic three point bending beams to measure the mechanical performance. (b) Representative force-displacement curves on unheated and laser heated beams to measure the stiffness of the material. It is observed that there is significant increase in the strength of the heated beam, since the ceramic component dominates the composition. (c) Front view of the configuration between the specimen and the indenter. (d) Characteristic stress-strain curves for the two samples for the same deformation length ( $5\ \mu\text{m}$ ). The ductile regime of the curve is significantly larger than the initial design. The reason is the increase of the post contact events in the proximal beams of the heated structure and the induced curvature of the internal beam members, which enhances the resilience of the structure to larger deformations. (e) SEM imaging of the initial FS structure after the indentation experiment. Buckled and fractured members can be observed, resulting in the subsequent instability (softening) of the structure during the plastic portion of the deformation. (f) SEM imaging of the heated FS structure after the indentation experiment. Fracture members are observed, as well as the curved members that contributed to the resilience of the structure to large deformations, manifested through the higher energy dissipation.

To experimentally validate the mechanical response, *in situ* SEM on microindentation tests were performed on single beam members and on the FS structure to measure the mechanical properties. By performing three point bending on the heated and unheated beam structures (figure 5(a)), the force displacement curves were obtained (figure 5(b)). Using static analysis of the bending moment diagram for the uniformly distributed load of the indenter, the Young's Modulus can be estimated to be 2.57 GPa and 4.92 GPa for the unheated and heated beams respectively. Therefore, the laser heating leads to 91% increase of the stiffness of the material. This result is congruous with the resilience obtained by the FEA, since the top layer is significantly stiffer. By performing uniaxial compression (figure 5(c)) on both heated and unheated samples, the obtained characteristic mechanical responses are presented in figure 5(d) (engineering stress-strain curves). The recordings of the deformations are presented in *VI-Recording 1* and

*VI-Recording 2*. It is evident that the energy dissipation of the heated structure, which is attained by calculating the area of the stress-strain curve, is substantially larger than the unheated one. More specifically, for the same amount of deformation, the heated sample has approximately two times higher energy dissipation. One reason for this is that to accomplish uniform shrinking of the upper layers, the internal beam members of the intertwined structure must also either bend or pre-buckle. As these beam members have sustained permanent deformation due to curvature, they are prestressed and therefore hardened. Consequently, they will require more mechanical energy to deform for the same amount of deformation as the straight ones. In addition, they are also in closer proximity to each other compared to the unheated ones. Hence, the increase of post contact events during large deformations will stiffen the structure. This result is consistent with the finite element analysis that was performed. These physical mechanisms that

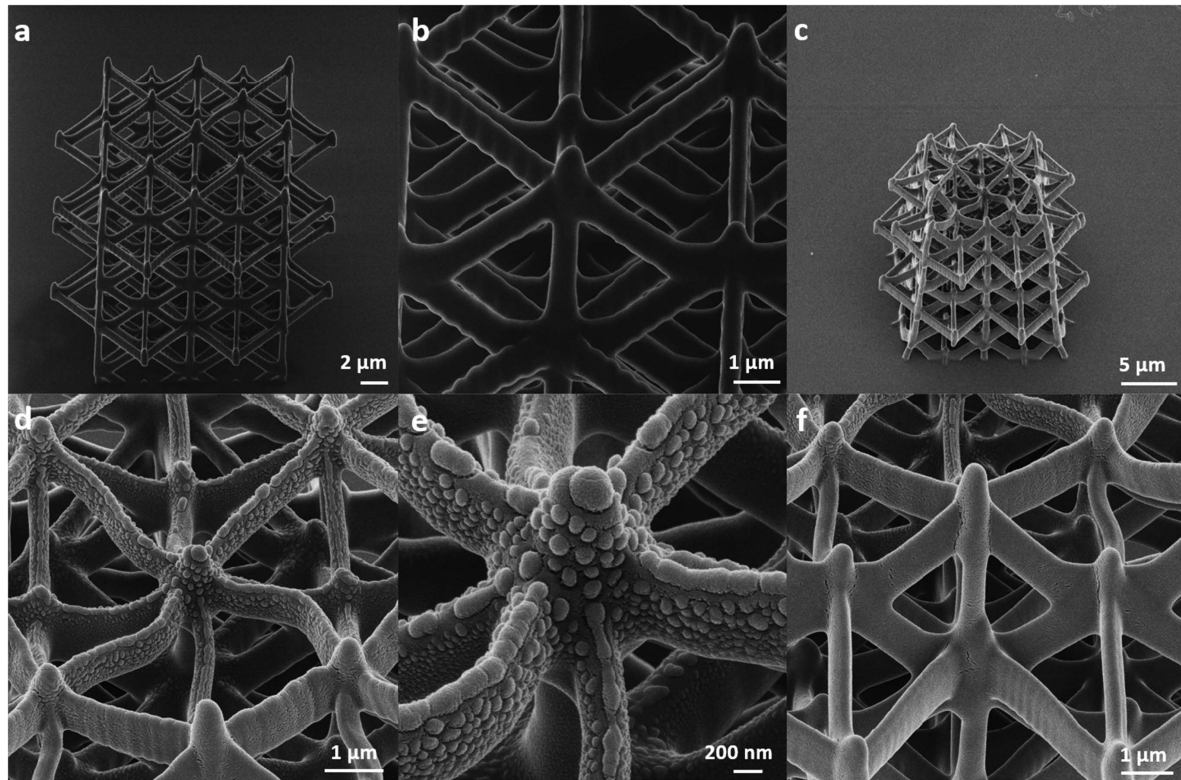


**Figure 6.** Helium Ion Microscopy characterization of unspattered and laser heated samples. (a) Unspattered FS structure. (b) Magnification on intersecting lattice members, revealing no nanoscale morphology of the surface of the lattices. (c) Isometric view of a laser heated structure at the center of the top layer. (d) Magnification in the center of the top layer, revealing a twist of the structure. (e) Higher magnification on the lattices, revealing the conglomeration and penetration of golden particles in the nanolattices. (f) The undistorted neighboring region that the laser beam has not affected.

are employed for this architectural design have been reported before [36]. However, the aforementioned repercussions of the heating enhanced these mechanisms even more. Furthermore, the local evaporation of the polymeric part of the beams increased the contribution of the ceramic part [2]. To validate this, EDS analysis was performed on the fractured cross sections of the tested unheated (figure S3) and heated structures (figure S4). The reason that EDS was performed after the mechanical testing was to avoid a potential chemical and structural alteration ushered by the focused ion beam (FIB). Again, we observe a decrease of carbon content from 42% to 27% on the heated member compared to the non-heated one and the relative ratio of all the other elements remained constant. This verifies that the laser heating renders the whole cross section ceramic and does not cause a surface effect only. In addition, the conglomeration of the coating particles is also evident in figures S4 and 6. To inspect these morphological features in extremely high resolution, Helium Ion Microscopy (HIM) was employed. HIM enables extremely high resolution of even nonconductive samples and imaging and characterization of nanometer features. Figure 6(a) reveals the unspattered structure, showing that the initial polymerized material has no nanoscale surface features at intersecting lattice members (figure 6(b)). Nevertheless, laser heating on the top layer precipitates a concave deformation of the structure, demonstrated in figure 6(c). Higher magnification on the

heated region elucidates a highly twisted structure with gold particles of 30–40 nm diameter penetrating the lattice members (figures 6(d)–(e)). In addition, this effect is constrained only in the regions that the laser beam heats, since there is no change in the morphology of the gold layer in the unheated regions (figure 6(f)). These findings bolster the argument of a hybrid structure.

In addition, the effect of multiple locally heated spots was investigated. To accomplish this, the laser beam was split utilizing a beam splitter and the two beams were focused on two different locations of the structure. Characteristic deformed morphologies are presented in figure S6. This process substantially narrows the threshold of the optimum laser parameters. Low laser power at 0.02 W does not accomplish large deformations, since the laser power is divided in the two spots (figure S6(b)). Hence, the blatant distortion and twist observed in the case of single laser heating is not significant. In addition, higher laser power at 0.05 W significantly damages the structure, since the gold layers melt (figure S6(b)), leading to even fracture of the beam members. Nevertheless, there is no large and uniform conglomeration of particles in the laser beam irradiated spots (figures S6(c)–(d)). To further investigate this effect, heat transfer simulations with two laser beams at different locations were performed (figure S7). While the temperature distribution is higher through the depth of the structure, it is also more uniform along the lattice members

of each layer. This indicated that while there will be large deformations through the whole structure, as observed in figure S6(b), the spatial temperature gradient on the horizontal plane is not large enough to cause large deformations as those incurred by a single laser beam (figure S6(a)). While this technique is significantly more challenging to realize complex morphologies like the ones of figure 3, it is imperative for the efficient design of large-scale structures. Hence, future work should aim on the optimization of the experimental parameters to accomplish complex but controllable topologies. It is conceivable that this can be accomplished by multiple laser beams acting on different areas of the specimen and operate either synchronously or separated temporally.

Based on the mechanical testing, there is an increase in the strength of material. Ductility and strength are competing mechanisms. Therefore, the trade-off is microscopic fracture of beam members, without the substantiation of buckling events as in the unheated sample (figures 5(e) and (f), and VI1 Recording 1 and VI2 Recording 2). Thus, from the standpoint of mechanical performance, this structure macroscopically combines both strength and ductility, ushering the potential utility of this technique for complex high energy dissipation nanocomposite materials with nanoscale features [42].

As the potential of this process was demonstrated, further research must be conducted to comprehend the laser selective carbonization under the scope of the desired mechanical performance. Detailed characterization of correlations between laser parameters and resulted geometries should also be pursued. Then thorough chemical composition details of heated specimen could be investigated by micro Raman spectroscopy [43] apart from EDS. A shrewd scheme of controlling the laser power, dwell time and scan path is required to implement the observed correlation. For a rarefied design challenge as this one, optimization techniques [44] and even data-driven methods like deep learning [45, 46] can be utilized to design the attainable structure as well as to attain the required laser paths to fabricate them. Moreover, this laser processing caused a distortion in the symmetry of the structures by the introduction of irregularities. These alterations constitute a major challenge in the analytical behavior of such structures. Nevertheless, stochastic methodologies have been demonstrated taking into account the several constituent representative unit cell elements and utilizing probabilistic descriptions of asymmetrical structures [47]. These models should be expanded in the 3D elasto-plastic mechanical behavior of metamaterial structures, providing a coherent framework to model and predict their mechanical response. These irregularities should also take into account the modified localized mechanical properties precipitated by the laser heating.

### 3. Conclusions

In summary, a novel post-processing procedure for the modification of the geometry and chemical composition of fabricated microstructures was presented. Laser-induced local extreme pyrolysis on polymeric structures introduced localized shrinking and ceramic-polymer hybrid composites.

Through furnace annealing, we estimate that the local temperature will reach 375 °C to provide the observed volume reduction in laser processing. With controlled fixed irradiation or laser scanning, complex curved and gradient geometries can be generated. Detailed mechanical simulations illuminate the deformation and predict the resulted mechanical performance. SEM micro-indentation analysis elucidated how the microscopic mechanical response was reflected on the stress-strain curve. The laser carbonized hybrid material combines enhanced macroscopic ductility and strength. Therefore, the present study provides the framework for using the laser to create hybrid structures with complex geometry and enhanced mechanical properties. Their utility could be employed for a plethora of applications, such as tailored scaffolds with stiffness gradient for artificial tissue modeling and stress distribution [8, 48] and 3D patterning of local hierarchical nanostructures for 3D complex biomimetic materials and structures [9, 10, 12, 14]. In addition, this process can provide more complex micro optical components fabricated by MPL [41] Finally, it promulgates new post-processing techniques that can be employed to accompany MPL for hybrid 3D nanoscale structures.

## 4. Methods

### 4.1. Materials

The metamaterial structures were made of a hybrid organic-inorganic material Zr-DMAEMA consisting of 70 wt% zirconium propoxide and 10 wt% (2-dimethylaminoethyl) methacrylate (DMAEMA) (Sigma-Aldrich). This material employs the diffusion-assisted high-resolution direct femto-second laser writing technique [20]. This method provides high spatial resolution, rigid and stable 3D architected geometries of high complexity, even when defects are introduced, distorting its periodicity [31]. As a first step, 1.4 ml of 3-(trimethoxysilyl)propyl methacrylate (MAPTMS) (Sigma-Aldrich) were mixed with 0.14 gr of hydrochloric acid in a vial. Then, 137.7  $\mu$ l DMAEMA were mixed with 0.66 ml zirconium (IV) propoxide (ZPO) solution with 70 wt% 1-propanol in another vial. After mixing both mixtures, they were placed in the same vial together with 0.016 gr of photoinitiator (4,4'-bis(diethylamino)benzophenone (Sigma-Aldrich). Before the fabrication of the structures, the material was placed onto glass substrates preserved at room temperature in vacuum for 16 h.

### 4.2. Microfabrication and laser extreme pyrolysis

Regarding the fabrication procedure the whole step-by-step process is delineated in figure 1. The experimental setup utilized for MPL presented in the SI (figure S7). The system includes a FemtoFiber pro NIR laser with a wavelength of 780 nm, pulse width of 100 fs, and repetition rate of 80 MHz. The beam is focused by a 100  $\times$  microscope objective lens (Plan-Apo Chromat 100  $\times$ /1.40 Oil M27, Zeiss). By tightly focusing the laser into the photosensitive material, the material is polymerized locally. The stage was then translated such

that the focused beam could ‘write’ inside the material and fabricate the desired 3D structure. Afterwards, to increase the absorbance of the material and increase the realm of the laser processing power, we gold sputtered the samples for 100 s. For the designated time, the thickness of the coating is 15 nm. Then, a CW laser (Lighthouse Sprout-C 4 W, 532 nm) is used to process the sample. A Mitutoyo APO 10X objective lens is utilized to focus the laser beam into a 6 $\mu$ m FWHM diameter. The in-situ video recording of the process is captured with a CCD camera from AmScope MD1000. The laser power for effective deformation was calibrated to be 5–10 mW depending on the heat dissipation of the processed target. For point irradiation, the laser dwell time is set to be 200 ms and for scanning, the speed is set to be 0.1 mm s<sup>-1</sup>. For the heating of the individual beam members, the same apparatus was employed with laser power equal to 10 mW. Higher laser powers lead to the ablation of the beam members. The laser beam was focused on the top of the beam member. By scanning the laser beam along the length of the beam member, uniform shrinkage of the cross section along the whole length was accomplished. In order to accomplish multiple locally heated spots in the structure, the laser beam was split using a beam splitter and utilizing a Mitutoyo APO 20X objective lens, two distinct laser beams with distance 10  $\mu$ m could simultaneously heat the structure.

#### 4.3. Finite element analysis on the mechanical behavior

The structural FEA simulations were performed with the multi-purpose finite element software ANSYS (Workbench 18.0). The selected material properties are in agreement with those obtained by the mechanical testing of the individual beam members. Specifically, the following beam properties were used in the FEA analysis: 2.57 GPa elastic modulus, 0.45 Poisson’s ratio, and 18 MPa yield strength. To compromise with the variation of the stiffness and strength due to the laser heating, these values were modelled to vary linearly with respect to the height of the geometry, up to the modulus equal to 4.92 GPa and strength equal to 70 MPa, by measuring the force displacement curves until fracture commenced. Since the heat transfer simulations revealed that the heat flux varies only when the beam power changes, it was modelled that individual beams would have a constant Young’s Modulus and Yield Strength along their length, whereas variation in these properties would occur when there is another beam along the height of the structure. Based on the SEM images and inspecting the altered geometry of the beam members with respect to the height of the structure it was selected that the stiffness step would be 0.1958 GPa, splitting the structure into 12 layers. It must be noted that these layers do not have the same height but divide the structure to regions of beam members with the similar dimensions. Hence, the top beam members would have modulus equal to 4.92 GPa, the ones below them 4.7242 GPa as so forth. The simulations presented in figure 4(b) were realized under these assumptions, while the simulation results of figure 4(a) were realized with the mechanical properties of the unheated material. The structures were discretized by 10-node, tetrahedral finite elements. The unheated structure was modeled with 394275 elements having 223200 nodes, whereas

the heated structure was modeled with 385250 elements having 221250 nodes. The boundary conditions were chosen to closely match those of the experiments. Because of the slightly thicker hinges connecting the beams, the indenter load was initially applied on the hinges. Thus, the compressive load of the microindenter was transmitted to the structure through these hinge points. For this reason, point–displacement boundary conditions were applied to the mesh nodes corresponding to the top face hinges. Since the bottom face of each structure is attached to the substrate, all the degrees of freedom of the bottom nodes were fully constrained. The ANSYS Design Modeler was used to design the structure geometries. The CAD model of the heated structure was based on the SEM imaging of the measured dimensions of the individual beam members.

#### 4.4. Mechanical testing

Regarding the mechanical testing apparatus, it consisted of a nanoindentation apparatus (TI 88 SEM PicoIndenter, Hysitron), inside a Scanning Electron Microscope (FEI Quanta 3D FEG) which enables high-precision nanomechanical testing and *in situ* recording of the deformation. The indentation tip was made from a Mo tip and it was cut using a femtosecond laser to have a 80  $\mu$ m diameter of the contact area. All of the fabricated arrays were designed such that the surface area of the periodic structure would be less than the contact area of the sample for uniform loading. Quasi-static experiments were performed with loading rate 200 nm s<sup>-1</sup> triangular loading profile to hamper creep during the indentation experiments.

#### 4.5. Chemical composition characterization

To evaluate the disparities in the chemical composition of the heated and unheated members, energy-dispersive x-ray spectroscopy (EDS) was employed on the simple triangular specimens and the indented FS structures before and after heat treatment. From the collected x-rays, the chemical composition distribution maps were obtained combined with the percentage of each elements comprising the structure. Regions with less density of a specific element will appear as ‘darker’ in the captured mapped region.

### Acknowledgments

This research was partially supported by the National Science Foundation (NSF) under the Scalable Nanomanufacturing (SNM) Program, Grand No. 1449305 and the Civil, Mechanical and Manufacturing Innovation (CMMI), Grand No. 1363392. The SEM, EDS, HIM and microindentation experiments are carried out at the California Institute of Quantitative Bioscience (QB3) in UC Berkeley. The authors thank Professor P. Hosemann, Department of Nuclear Engineering, University of California, Berkeley, for using the microindentation apparatus. The authors thank Dr. Frances Allen, Department

of Materials Science and Engineering, University of California, Berkeley, for the training on the Helium Ion Microscope. The authors also thank Matthew Eliceiri of the Laser Thermal Lab, UC Berkeley, for assisting in the simultaneous local laser heating of the structures.

## Author Contributions

Z.V. and L.W. conceived the idea, L.W. designed and implemented the laser and furnace pyrolysis experiments. Z.V. designed and fabricated the structures through MPL and implemented the mechanical testing experiments and HIM imaging. Z.V. performed the mechanical analysis. L.W. performed the heat transfer simulations. Both Z.V. and L.W. contributed to the geometry and composition characterization, as well as the analysis of the results. C.G. supervised and supported the work. All authors contributed in the preparation of the manuscript.

## ORCID iDs

Zacharias Vangelatos  <https://orcid.org/0000-0001-9513-3671>

Costas P Grigoropoulos  <https://orcid.org/0000-0002-8505-4037>

## References

- [1] Bauer J, Meza L R, Schaedler T A, Schwaiger R, Zheng X, Valdevit L 2017 Nanolattices: an emerging class of mechanical metamaterials *Adv. Mater.* **29** 1701850
- [2] Zhang X, Wang Y, Ding B, Li X 2019 Design, fabrication, and mechanics of 3D Micro-/Nanolattices *Small* **19** 02842
- [3] Berezovski A, Yildizdag M E, Scerrato D 2018 On the wave dispersion in microstructured solids *Continuum Mech. Thermodyn.* (<https://doi.org/10.1007/s00161-018-0683-1>)
- [4] Xu C, Gallant B M, Wunderlich P U, Lohmann T, Greer J R 2015 Three-dimensional Au microlattices as positive electrodes for Li–O<sub>2</sub> Batteries *ACS Nano* **9** 5876–83
- [5] Cui H, Hensleigh R, Yao D, Maurya D, Kumar P, Kang M G, Priya S, Zheng X R 2019 Three-dimensional printing of piezoelectric materials with designed anisotropy and directional response *Nat. Mater.* **18** 234–41
- [6] Fu H *et al* 2018 Morphable 3D mesostructures and microelectronic devices by multistable buckling mechanics *Nat. Mater.* **17** 268–76
- [7] Kolken H M A, Janbaz S, Leeftang S M A, Lietaert K, Weinans H H, Zadpoor A A 2018 Rationally designed meta-implants: a combination of auxetic and conventional meta-biomaterials *Mater. Horiz.* **5** 28–35
- [8] Ma Z, Huebsch N, Koo S, Mandegar M A, Siemons B, Boggess S, Conklin B R, Grigoropoulos C P, Kevin E 2018 Healy, Contractile deficits in engineered cardiac microtissues as a result of MYBPC3 deficiency and mechanical overload *Nat. Biomed. Eng.* **2** 955–67
- [9] Gao H, Ji B, Jäger I L, Arzt E, Fratzl P 2003 Materials become insensitive to flaws at nanoscale: lessons from nature *PNAS* **100** 5597–600
- [10] Sun Z, Liao T, Liu K, Jiang L, Kim J H, Dou S X 2014 Fly-eye inspired superhydrophobic anti-fogging inorganic nanostructures *Small* **10** 3001–6
- [11] Ritchie R O, Buehler M J, Hansma P 2009 Plasticity and toughness in bone *Phys. Today* **62** 41–47
- [12] Liu Z Q, Zhang Z F, Ritchie R O 2018 On the materials science of nature's arms race *Adv. Mater.* **30** 16
- [13] Quan H, Yang W, Schaible E, Ritchie R O, Meyers M A 2018 Novel defense mechanisms in the armor of the scales of the "living fossil" coelacanth fish *Adv. Funct. Mater.* **28** 1804237
- [14] Luo S, Greer J R 2018 Bio-mimicked silica architectures capture geometry, microstructure, and mechanical properties of marine diatoms *Adv. Eng. Mater.* **20** 1800301
- [15] Sakellari I, Kabouraki E, Gray D, Purlys V, Fotakis C, Pikulin A, Bityurin N, Vamvakaki M, Farsari M 2012 Diffusion-assisted high-resolution direct femtosecond laser writing *ACS Nano* **6** 2302–11
- [16] Ovsianikov A *et al* 2008 Ultra-low shrinkage hybrid photosensitive material for two-photon polymerization microfabrication *ACS Nano* **2** 2257–62
- [17] Manousidaki M, Papazoglou D G, Farsari M, Tzortzakis S 2019 Long-scale multiphoton polymerization voxel growth investigation using engineered Bessel beams *Opt. Mater. Express* **9** 2838–45
- [18] Gailevicius D, Padolskyte V, Mikoliunaite L, Sakirzanovas S, Juodkazis S, Malinauskas M 2019 Additive-manufacturing of 3D glass-ceramics down to nanoscale resolution *Nanoscale Horiz.* **4** 647–51
- [19] Jonusauskas L, Gailevicius D, Rekstyte S, Baldacchini T, Juodkazis S, Malinauskas M 2019 Mesoscale laser 3D printing *Opt. Express* **27** 15205–21
- [20] Wollhofen R, Katzmann J, Hrelescu C, Jacak J, Klar T A 2013 120 nm resolution and 55 nm structure size in STED-lithography *Opt. Express* **21** 10831–1084
- [21] Cui H, Hensleigh R, Chen H, Zheng X 2018 Additive manufacturing and size-dependent mechanical properties of three-dimensional microarchitected, high-temperature ceramic metamaterials *J. Mater. Res.* **33** 360–71
- [22] Oakdale J S *et al* 2017 Direct laser writing of low-density interdigitated foams for plasma drive shaping *Adv. Funct. Mater.* **27** 1702425
- [23] Wang H *et al* 2017 Ultralight, scalable, and high-temperature-resilient ceramic nanofiber sponges *Sci. Adv.* **3** e1603170
- [24] Ma Q, Dutta S, Wu K C-W, Kimura T 2018 Analytical understanding of the materials design with well-described shrinkages on multiscale *Chem. Eur. J.* **24** 6886–904
- [25] Bauer J, Schroer A, Schwaiger R, Kraft O 2016 Approaching theoretical strength in glassy carbon nanolattices *Nat. Mater.* **15** 438–43
- [26] Mieszala M, Hasegawa M, Guillonneau G, Bauer J, Raghavan R, Frantz C, Kraft O, Mischler S, Michler J, Philippe L 2017 Micromechanics of amorphous metal/polymer hybrid structures with 3D cellular architectures: size effects, buckling behavior, and energy absorption capability *Small* **13** 1602514
- [27] Johnson R W, Hultqvist A, Bent S F 2014 A brief review of atomic layer deposition: from fundamentals to applications *Mater. Today* **17** 236–46
- [28] Xia X, Afshar A, Yang H, Portela C M, Kochmann D M, Di Leo C V, Greer J R 2019 Electrochemically reconfigurable architected materials *Nature* **573** 205–13
- [29] Vangelatos Z, Komvopoulos K, Grigoropoulos C P 2018 Vacancies for controlling the behavior of microstructured three-dimensional mechanical metamaterials *Math. Mech. Solids* **24** 511–24
- [30] Pham M-S, Liu C, Todd I, Lertthanasarn J 2019 Damage-tolerant architected materials inspired by crystal microstructure *Nature* **565** 305–11

- [31] Elmadih W, Syam W P, Maskery I, Chronopoulos D, Leach R 2019 Mechanical vibration bandgaps in surface-based lattices *Addit. Manuf.* **25** 421–9
- [32] Kevin J, Marcus H L 1995 Silicon carbide from laser pyrolysis of polycarbosilane *J. Am. Ceram. Soc.* **78** 2263–6
- [33] Mantese J V, Catalan A B, Sell J A, Meyer M S, Mance A M 1990 Selective laser pyrolysis of metallo-organics as a method of forming patterned thin film superconductors U.S. Patent No. 4916115
- [34] Lin J, Peng Z, Liu Y, Ruiz-Zepeda F, Ye R, Samuel E L G, Jose Yacaman M, Yakobson B I, Tour J M 2014 Laser-induced porous graphene films from commercial polymers *Nat. Commun.* **5** 5714
- [35] Luo S, Hoang P T, Liu T 2016 Direct laser writing for creating porous graphitic structures and their use for flexible and highly sensitive sensor and sensor arrays *Carbon* **96** 522–31
- [36] Vangelatos Z, Melissinaki V, Farsari M, Komvopoulos K, Grigoropoulos C 2019 Intertwined microlattices greatly enhance the performance of mechanical metamaterials *Math. Mech. Solids* **24** 2636–48
- [37] Schroer A, Wheeler J M, Schwaiger R 2018 Deformation behavior and energy absorption capability of polymer and ceramic-polymer composite microlattices under cyclic loading *J. Mater. Res.* **33** 274–89
- [38] Parida O P, Bhat N 2009 Characterization of optical properties of SU-8 and fabrication of optical components *Int. Conf. on Optics Photonics* pp 4–7
- [39] Yang Y, Song X, Li X, Chen Z, Zhou C, Zhou Q, Chen Y 2018 Recent progress in biomimetic additive manufacturing technology: from materials to functional structures *Adv. Mater.* **30** 1706539
- [40] Tsutsumi N, Hirota J, Kinashi K, Sakai W 2017 Direct laser writing for micro-optical devices using a negative photoresist *Opt. Express* **25** 31539–51
- [41] Gao L et al 2018 High-entropy alloy (HEA)-coated nanolattice structures and their mechanical properties *Adv. Eng. Mater.* **20** 1700625
- [42] Wu W, Hu W, Qian G, Liao H, Xu X, Berto F 2019 Mechanical design and multifunctional applications of chiral mechanical metamaterials: A review *Mater. Des.* **180** 107950
- [43] Kuo -C-C 2019 Micro-Raman spectroscopy characterization of polycrystalline silicon films fabricated by excimer laser crystallization *Opt. Lasers Eng.* **47** 612–16
- [44] Chen D, Skouras M, Zhu B, Matusik W 2018 Computational discovery of extremal microstructure families *Sci. Adv.* **4** eaac7005
- [45] Nadell C C, Huang B, Malof J M, Padilla W J 2019 Deep learning for accelerated all-dielectric metasurface design *Opt. Express* **27** 27523–35
- [46] Ma W, Cheng F, Liu Y 2018 Deep-learning-enabled on-demand design of chiral metamaterials *ACS Nano* **12** 6326–34
- [47] Mukhopadhyay T, Adhikari S 2017 Stochastic mechanics of metamaterials *Compos. Struct.* **162** 85–97
- [48] Pennacchio F A, Caliendo F, Iaccarino G, Langella A, Siciliano V, Santoro F 2019 Three dimensionally patterned scaffolds modulate the biointerface at the nanoscale *Nano Lett.* **19** 5118–23